



ARTICLE

<https://doi.org/10.1038/s42004-019-0200-x>

OPEN

Direct measurements of semi-volatile organic compound dynamics show near-unity mass accommodation coefficients for diverse aerosols

Xiaoxi Liu ¹, Douglas A. Day¹, Jordan E. Krechmer^{1,2}, Wyatt Brown¹, Zhe Peng ¹, Paul J. Ziemann¹ & Jose L. Jimenez¹

The partitioning of low- and semi-volatile organic compounds into and out of particles significantly influences secondary organic aerosol formation and evolution. Most atmospheric models treat partitioning as an equilibrium between gas and particle phases, despite few direct measurements and a large range of uncertain mass accommodation coefficients (α). Here we directly measure the dynamic, isothermal partitioning of specific organic compounds using mass spectrometry in a Teflon chamber. Measurements are conducted under dry and humid conditions using seeds of different properties that are atmospherically relevant. α values determined independently from gas- and particle-phase observations are consistent and average 0.88 ± 0.33 for all the studied seeds and probe gases. Our results also imply fast mixing, within ~ 200 s, between dry α -pinene/ O_3 SOA and the oxidized compounds. These results indicate that mass transfer limitations in the atmosphere may be less important than some recent studies suggest.

¹Cooperative Institute for Research in Environmental Sciences (CIRES) and Department of Chemistry, University of Colorado Boulder, Boulder CO, USA. ²Present address: Aerodyne Research Inc., Billerica, MA, USA. Correspondence and requests for materials should be addressed to J.L.J. (email: jose.jimenez@colorado.edu)

Organic aerosols (OA) represent a major fraction of the mass of submicron aerosol in Earth's atmosphere^{1,2}. OA worldwide is dominated by secondary organic aerosols (SOA), which are formed in the atmosphere from the condensation of low-volatility and semi-volatile organic compounds (L/SVOCs)^{1–4}. Gas/particle (G/P) partitioning of organic species is generally modeled using equilibrium absorptive partitioning theory^{5,6}. The theory states that at equilibrium, the fraction of SVOCs in the particle phase (F_p) depends on their pure-compound volatilities (c^*), compound activity coefficient (γ), and total OA mass concentration (c_{OA}) present. In an aerosol mixture, γ modifies c^* to give the effective saturation concentration (c_{eff}^*) of the compound.

$$F_p = \left(1 + \frac{\gamma c^*}{c_{OA}}\right)^{-1} = \left(1 + \frac{c_{eff}^*}{c_{OA}}\right)^{-1}. \quad (1)$$

In a more detailed kinetic representation, the mass accommodation coefficient (α) is a critical parameter that describes the fraction of vapor molecules taken up by the particle phase for each vapor collision with a particle. The value of α determines if partitioning is kinetically limited and impacts the G/P equilibration timescale in the atmosphere. $\alpha = 1$ indicates no mass transfer limitations from vapors to the condensed phase. In atmospheric models, SOA is typically modeled by assuming instantaneous equilibration between gases and particles^{7,8}. In some models that simulate SVOC condensation kinetically, proper consideration of kinetic limitations often lacks⁹. Previous determinations of α for organic vapors onto particles range from near 1 to as low as 0.001^{10–21}. During the complex process of gas molecule incorporation into the bulk of condensed phase, the properties of aerosol particles can affect the magnitude of α . Recent studies show that SOA in the atmosphere can in some cases exist in a highly viscous semisolid (glassy) or solid state, which could retard molecular diffusion within the aerosol matrix, resulting in an *apparent* $\alpha < 1$ ^{22–24}. In contrast, there has been field and laboratory work showing that at least some ambient and biogenic SOA does not appear to significantly resist the exchange of semivolatile compounds and exhibits mixing times < 1 h under typical boundary layer conditions^{14,25–28}. However, the above-mentioned studies have used indirect methods, such as measuring evaporation rates (sometimes at high temperatures) and viscosity, and have been limited to only particle characterization, while the direct measurement of gas- and particle-phase concentrations of specific molecules during the dynamic partitioning process had not been demonstrated until recently. On the other hand, in organic/inorganic and hydrophilic/hydrophobic organic mixtures, particle morphology, such as liquid–liquid phase separation, can also affect the equilibration rates and the thermodynamics of molecules partitioning through phases^{29,30}. Recently, Krechmer et al. determined α for partitioning of oxidized compounds to dioctyl sebacate (DOS) particles in a Teflon chamber by directly measuring and modeling the vapor concentration evolution³¹. They found an average α of 0.7 for L/SVOCs with saturation concentrations ranging from 10^{-3} to $10^2 \mu\text{g m}^{-3}$. Given that α could be different for different particle substrates, there is need to quantify α for atmospherically relevant particles with different phases and properties using the experimental techniques that are capable of fast, direct measurement. A better understanding of α also helps constrain the timescales of partitioning from ~ 1 min ($\alpha = 1$) to many hours ($\alpha = 0.001$) at typical atmospheric aerosol loadings. The atmospheric models' instant G/P equilibration assumption may become inappropriate if this timescale is relatively long compared with other simulated processes.

A number of advances in speciation of compounds relevant to G/P partitioning for SOA have been achieved by new developments in instrumentation for laboratory and field studies^{27,32–37}. Among these techniques, gas-phase species-level concentrations can be rapidly monitored in situ using the soft ionization mass spectrometry^{27,36,38}. Measurements of particle-phase speciation and concentrations often suffer from slower time resolution (~ 1 h) due to the need of aerosol collection on a filter, and/or thermal decomposition when thermal desorption of OA is required^{27,32–34,37}. The recently developed technique of extractive electrospray ionization (EESI) provides soft ionization of many organic molecules in real time with minimum sample heating^{39,40} and has been very recently improved to achieve higher sensitivities, making it now possible to be applied to ambient-level concentrations⁴¹. These qualities make EESI, when coupled with an inlet that sufficiently removes the gas phase, well-suited for fast online analysis of OA, as in partitioning kinetic measurements.

This study quantifies the mass accommodation coefficients of L/SVOC species into a variety of preexisting particles of different phases and properties: liquid organics, including oleic acid, squalane, and pentaethylene glycol; solid seeds, including ammonium sulfate (AS) and sucrose; liquid inorganic, including deliquesced AS; and α -pinene/ O_3 SOA that represents a realistic atmospheric SOA mixture. We use a well-characterized, relatively simple gas-phase chemical system to rapidly produce L/SVOCs in 10 s, which are then taken up by particles and the chamber walls at a slower timescale of ~ 2 min and ~ 17 min, respectively. Chemically speciated gas-phase products are monitored by a chemical ionization mass spectrometer (CIMS) coupled with a NO_3^- source (NO_3^- -CIMS), while an EESI-MS measures the same molecules in the particle phase as they partitioned into the aerosol. By simultaneously fitting gas/particle/wall partitioning with a kinetic box model, we can provide robust constraints on α . We also discuss the implications of our findings to atmospheric partitioning.

Results

SOA formation overview. Details of the experiments, including procedures, instruments, measurements, and partitioning processes, are described in “Methods” section and summarized in Supplementary Fig. 1. In short, the partitioning L/SVOCs were produced by a fast (10 s) OH oxidation of alkanols under high NO. The multifunctional products that were monitored by real time mass spectrometry and used to derive α include dihydroxynitrates (DHNs), trihydroxynitrates (THNs), and carbonyl dihydroxynitrates (CDHNs) (Supplementary Table 1)⁴².

In our seeded experiments (Supplementary Table 2), as well as the DOS seed experiments of Krechmer et al.³¹, SOA volume formed by the partitioning of these L/SVOCs usually peaked within 2–3 min of the OH pulse. Since the L/SVOC vapor wall loss timescale for this chamber is ~ 17 min, the initial SOA formation is dominated by G/P partitioning with little wall effects. Typically, peak SOA volume ranged from 2.5 to $11 \mu\text{m}^3 \text{cm}^{-3}$ (smaller than or similar to the seed volumes) depending on the preexisting seed type (Supplementary Fig. 2). Note that the differences in SOA mass across seed types are generally larger than the variability within the same seed (even when combining same-seed experiments with different condensation sink, or CS), owing to thermodynamic differences in partitioning among seeds. The oxidized L/SVOCs then continued re-partitioning among phases. Since the vapor-phase L/SVOCs were lost to chamber walls, which have a large equivalent mass concentration (C_w , Supplementary Fig. 3) but a slower timescale, the net effect of this “wall denuding” is a constantly decreasing aerosol volume with time (even when corrected for particle-wall losses). After 1 h, the

fraction of evaporated SOA spanned from ~12% (oleic acid) to over 90% (sucrose) of the initially formed mass concentrations (Supplementary Fig. 2). The SOA amount formed and lost is likely affected by varying activity coefficients of the L/SVOCs in different seeds, which are influenced by the aerosol mixture composition. For almost all seed types, we measured OA composition using an aerosol mass spectrometer (AMS)^{43,44}. The SOA mass spectra of all available experiments show consistent composition (Supplementary Fig. 2 and Table 3). In addition, SOA analysis performed using liquid chromatography and online and offline mass spectrometry methods similar to those used previously indicate that the SOA products are similar to those formed from the reaction of linear alkanes but with an additional hydroxyl group, as expected^{42,45,46}. The major SOA products are DHNs, with a minor contribution from cyclic hydroxy hemiacetals.

This work examines the determined α values, which are predominantly constrained by the time evolution over the first ~20 min, when condensation to particles was the dominant partitioning flux and partitioning to the walls was slow.

Partitioning kinetics of gas-phase L/SVOCs. We first present results of condensation measured by NO_3 -CIMS. In a seeded experiment, vapors condense to both particle CS and chamber walls. As condensation proceeds, these two reservoirs start to act as two sources as vapors re-evaporate at volatility-dependent rates, until a steady state is reached. In the experiment with the smallest seed concentration (~1.8 $\mu\text{g m}^{-3}$ of oleic acid) L/SVOCs reach a steady state in less than 400 s, ~2.5 times faster than the gas-wall equilibrium timescale. Thus in all our experiments, the processes of vapor uptake into particles versus walls can be readily separated due to the difference in their timescales. In addition, we limited the analysis to experiments below an initial surface area of ~2500 $\mu\text{m}^2/\text{cm}^3$. As aerosol surface area increases, the rate coefficient of gases condensing on particles ($k_{G \rightarrow P}$) increases, which results in gaseous concentrations decaying at higher rates. Therefore, at very high surface areas, it is possible that L/SVOCs condensed so fast that the CIMS may not be able to capture the true peak immediately after oxidation, leading to less precise and possibly low-biased condensing rates. An example of the time evolution of $\text{C}_8\text{H}_{17}\text{NO}_6$ THNs in the presence of oleic acid seed aerosol with varying seed concentrations is shown in Supplementary Fig. 4. As oleic acid increased from 148 to 622 $\mu\text{m}^2/\text{cm}^3$, the time that the THNs decayed to equilibrium shortened from ~550 s to ~250 s. This surface area dependence was observed for other seed types and also in previous studies³¹.

As shown in Supplementary Table 2, experiments with surface areas ~400–650 $\mu\text{m}^2/\text{cm}^3$, a relatively narrow range, were conducted for almost all seeds. Figure 1 shows gaseous time evolution of $\text{C}_6\text{H}_{13}\text{NO}_6$ THNs in the presence of different seed aerosol types that were mostly within this surface area range. We observed similar equilibrium timescales, 300–500 s, for all seeds. This indicates that α values, which characterize the condensation kinetics, are likely of the same order for this wide range of seeds. In the final steady state, the compounds exhibited different gas-phase concentrations. According to partitioning theory (Eq. 1), equilibrium gas concentration is affected by available c_{OA} and the activity coefficient (γ) of the L/SVOC in the seed/SOA mixtures. After accounting for c_{OA} , variation of γ across seeds is apparent in this dataset and explains the differences in steady-state gas concentrations. This variability is consistent with previous results^{47,48}.

Partitioning kinetics of particle-phase L/SVOCs. An important experimental advance made in this study was to use EESI-MS for

the real-time monitoring of some of the same L/SVOCs as they partitioned to the particle phase. Figure 2a shows a SOA mass spectrum obtained at the maximum SOA mass concentration, which contains mainly DHNs and is consistent with the other SOA composition measurements mentioned earlier. THNs were also detected (see “Methods” section for details).

We selected two pentaethylene glycol experiments with similar initial surface areas to compare gas and particle measurements. As shown in Fig. 2b, as gas phase $\text{C}_9\text{H}_{19}\text{NO}_5$ and $\text{C}_{12}\text{H}_{25}\text{NO}_5$ DHNs decayed, their particle-phase counterparts accumulated concurrently. Both phases reached equilibrium slightly after 200 s.

Values of α consistent with the experiments. By fitting the kinetic box model to the gas-phase measurements it was possible to constrain α and effective saturation concentrations (c_{eff}^*) for each measured L/SVOC in the presence of every seed. Details of the fitting can be found in “Methods” section and examples are shown in Supplementary Fig. 5 along with sensitivity tests performed using different sets of α and c_{eff}^* . As shown, reducing α from 1.0 to 0.1 leads to a much slower decay than observed. Furthermore, since c_{eff}^* determines the equilibrium concentration, higher c_{eff}^* would lead to higher gas concentration than observed. Note that our method successfully separated the effects of α and c_{eff}^* on partitioning. Regarding diffusivity, our model does not consider diffusion within the particles explicitly. Rather, we consider the two extremes of fast diffusion (and thus the whole particle is available for partitioning, i.e., $c_{\text{OA}} = c_{\text{seed}} + c_{\text{SOA}}$) and very slow diffusion (and thus only the layer of newly condensed SOA is available for partitioning, i.e., $c_{\text{OA}} = c_{\text{SOA}}$). The value of α is still the probability of uptake upon collision, and the availability of partitioning mass (and thus the diffusion coefficient of the seed) is then reflected on c_{eff}^* and the evaporation rate. Liquid organics were all assumed to have fast diffusion while solid AS and sucrose seeds were assumed to have no diffusion of SOA into the seed. The treatment of α -pinene/ O_3 SOA will be discussed in detail in the next section.

The optimal α and c_{eff}^* of all studied L/SVOCs (Supplementary Table 1) for all CIMS experiments are shown in Fig. 3a. Example error bars are shown for several L/SVOCs spanning the volatility range. Also plotted for comparison are α values for the same L/SVOC species determined from previous DOS seed experiments³¹. Since the upper limit of α was not constrained, a few model fittings generated α slightly >1, which is not physically possible. However, the error bars, which reflect uncertainties in parameters, SMPS measurements, and fitting (see “Methods” section), suggest that those values are not statistically >1 or indicative of any bias or artifact in the determination. The overall CIMS-determined average α for each seed range from 0.8 (± 0.4) to 1.0 (± 0.3), close to the average $\alpha = 0.7$ for DOS. In the volatility range of 10^{-2} – $1 \mu\text{g m}^{-3}$, α values clustered tightly around 0.5–1.0. As volatility increases beyond $10 \mu\text{g m}^{-3}$, higher variability in α was observed, accompanied by relatively larger error bars. Since these more volatile compounds partition less into the particle phase and the NO_3 -CIMS technique has lower sensitivity towards them, their measured decays have less contrast and the data have lower CIMS signal-to-noise (S/N) ratios, resulting in larger uncertainties.

We also used the box model to find the optimum α by fitting the EESI-MS observations while constraining c_{eff}^* using CIMS-determined values (Supplementary Fig. 5) since these are the best available estimates for c_{eff}^* under our conditions. Since the accuracy of c_{eff}^* can affect the fitted α , we performed sensitivity tests by multiplying/dividing c_{eff}^* by 10, which is much larger than the estimated $\pm 35\%$ uncertainty and the differences between c_{eff}^* and c_{SIMPOL}^* in most cases (Supplementary Fig. 6). Those changes

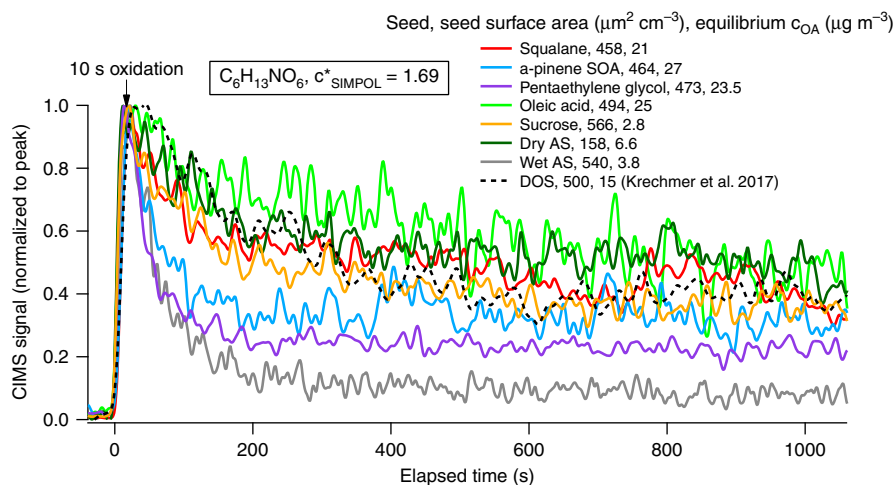


Fig. 1 Time evolution of $\text{C}_6\text{H}_{13}\text{NO}_6$ THNs measured by NO_3 -CIMS. In the presence of a variety of seed aerosols, the THNs condense at similar rates for similar starting surface areas, but equilibrate at different gas-phase concentrations depending on available c_{OA} (listed numbers measured at ~ 800 s) and activity coefficients at equilibrium. Note that the experiments shown have similar initial CS timescales (63–192 s, Supplementary Table 2), significantly slower than the 10 s oxidation, so the measured maximum peaks may slightly underestimate the peak gas-phase concentrations by up to $\sim 15\%$, as a ratio of the two timescales. All traces have been binomially smoothed across 20 1-s points for visual clarity and scaled to the maximum for comparison. Mass concentrations of α -pinene/ O_3 SOA were included in c_{OA}

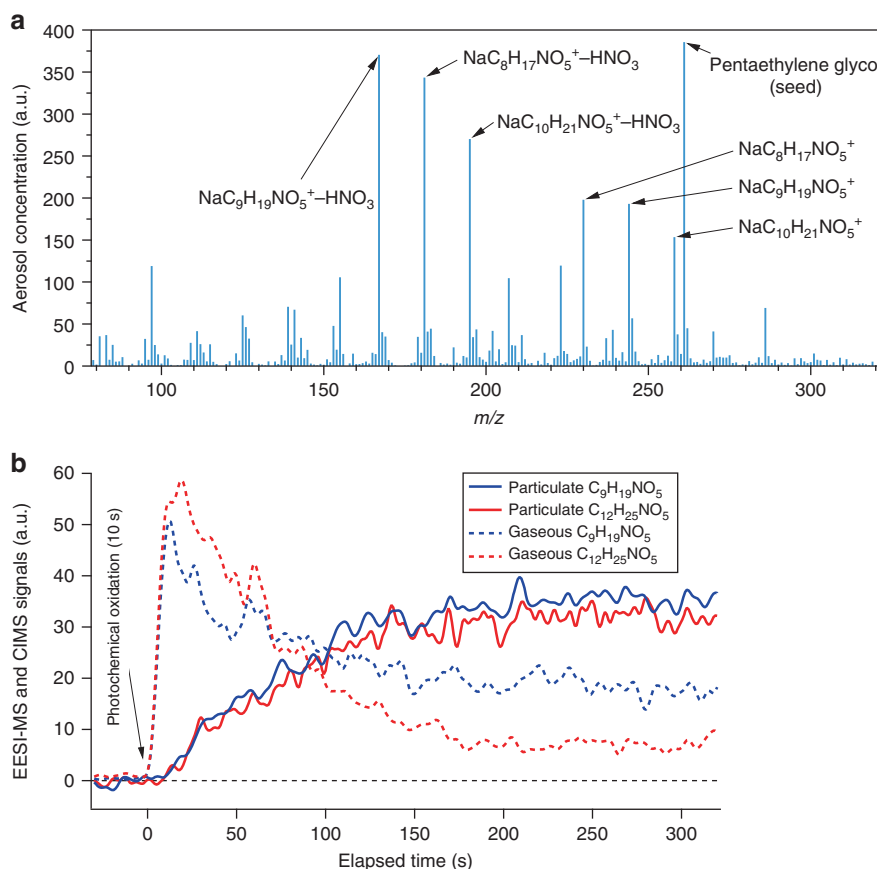


Fig. 2 EESI-MS real-time measurements. **a** Example SOA mass spectrum measured by EESI-MS, highlighting the pentaethylene glycol seed, and the main DHN aerosol products (Na^+ adducts and the adducts after a loss of HNO_3 fragment during ionization). **b** Time series of CIMS gas-phase and EESI-MS aerosol measurements of two DHNs that partitioned from gas-to-particle (pentaethylene glycol) phase. The partitioning timescales (~ 200 s) are consistent for both phases with similar initial surface areas (231 and $171 \mu\text{m}^2/\text{cm}^3$ for CIMS and EESI-MS experiments, respectively)

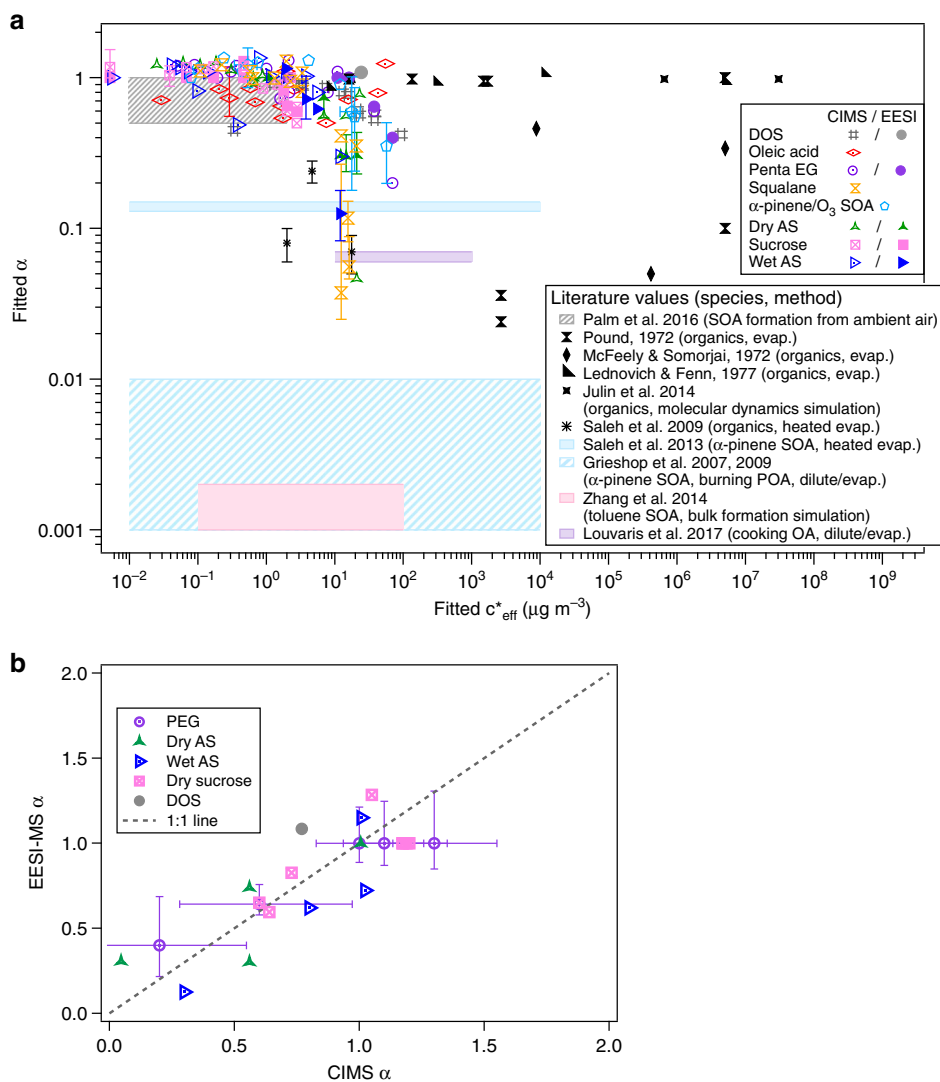


Fig. 3 Optimal α and c_{eff}^* . **a** Mass accommodation coefficients (α) of DHNs, THNs, and CDHNs determined in this study plotted as a function of model-determined c_{eff}^* . Note that the model-determined overall c_{eff}^* range varies across seeds, indicating differences in activity coefficients (γ). Literature values include α determined for SOA formed from oxidation of ambient precursors, pure liquid organics, α -pinene/ O_3 SOA, combustion and cooking aerosol, and toluene/OH SOA^{10–20}. **b** Comparison of α determined from model fitting of EESI-MS and CIMS measurements for the same compounds and seeds. Example error bars are shown, which reflect uncertainties in parameters, SMPS measurements, and fitting

resulted in α decreasing by up to a factor of 2 for $10 \times c_{\text{eff}}^*$ or increasing by up to $\sim 15\%$ for $c_{\text{eff}}^*/10$ for the most volatile C_6 – C_9 DHNs while α was nearly unchanged for the other less-volatile DHNs and THNs. Still, even with these perturbations the fitted α obtained from EESI-MS measurements ranged from ~ 0.5 to 1.0. The values of α determined from fitting the model to gas and particle measurements are consistent (Fig. 3b), and both indicate that α is near unity across a wide variety of seeds.

For the more volatile range of $c_{\text{eff}}^* > 10 \mu\text{g m}^{-3}$, our α values fall within the range measured in previous studies (Fig. 3a, b), and there is no conclusive dependence of α on a single property of the partitioning compounds, such as volatility or polarity.

Mixing with α -pinene/ O_3 SOA. α -pinene/ O_3 SOA, a representative atmospheric SOA mixture in locations subject to biogenic emissions, also shows the ability to rapidly take up the studied L/SVOCs. Since α -pinene/ O_3 SOA formed under dry conditions has high viscosity²³, we determined α and c_{eff}^* by either including or excluding α -pinene/ O_3 SOA in the partitioning c_{OA}^* (Eqs 1 and 5), and thus treating it as either liquid or solid.

Treating α -pinene/ O_3 SOA as a liquid assumes that dry α -pinene/ O_3 SOA takes up vapors like a liquid organic despite being viscous. This assumption yields reasonable results (Fig. 3a). But when treated as a solid the initial evaporation rates of the more volatile DHNs and C_6 THN (with fitted $c_{\text{eff}}^* > 1 \mu\text{g m}^{-3}$) are too fast, so that neither $\alpha = 1$ nor even an unrealistic $\alpha = 10$ can reproduce the observed, fast gas-phase decay (Fig. 4 and Supplementary Fig. 7). Although our model did not explicitly include particle-phase diffusion, the above sensitivity test indicates no kinetic limitation of uptake by dry α -pinene/ O_3 SOA due to surface accommodation or particle-phase diffusion. Diffusion of L/SVOCs within the near-surface layers of and possibly the entire particle probably occurs on a timescale of ~ 200 s, as this is the timescale of vapor condensation (Fig. 4). Consistent with our observation, Ye et al.²⁵ found that α -pinene/ O_3 SOA took up L/SVOCs evaporated from toluene/OH SOA without evidence of a mixing limitation, whereas Robinson et al. found that when squalane particles were coated with α -pinene/ O_3 SOA formed under dry conditions (RH = 5%) most squalane was able to evaporate, indicating that the α -pinene/ O_3 SOA shell did not

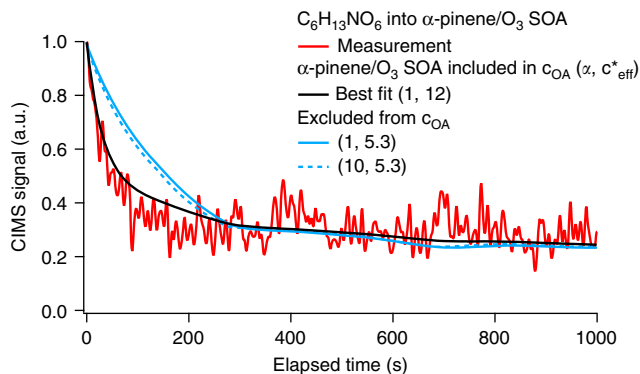


Fig. 4 Measured and modeled $C_6H_{13}NO_6$ THNs partitioning into α -pinene/ O_3 SOA. The model assumes $\alpha = 1$ that the SOA is either liquid or solid by including or excluding the SOA in the partitioning c_{OA} , respectively. Modeled concentrations and fluxes in all phases are shown for both assumptions in Supplementary Fig. 7

inhibit mass transfer⁴⁹. Saha and Grieshop⁵⁰ and Saleh et al.¹⁴ reported evaporation coefficients for dry ($RH < 10\%$) α -pinene/ O_3 SOA on the order of 0.1. In contrast, some studies found much slower evaporation and/or smaller α for dry α -pinene/ O_3 SOA and have attributed the reason to mass transfer limitations in a highly viscous or glassy amorphous state^{11,24}. Without simultaneously constraining the volatility of the SOA components, the slower evaporation rates may instead be limited by the presence of very low-volatility materials rather than high viscosity. Note that in the atmosphere, since OA can undergo further oxidation and/or heterogeneous reactions, ambient α -pinene/ O_3 SOA may have different viscosities from that generated in laboratory.

α for toluene SOA. The methods for quantifying α can also be applied to other chemical systems. By conducting 20 s burst of OH oxidation of toluene under high NO, we determined $0.3 \leq \alpha \leq 0.6$ for SOA-forming L/SVOCs based on AMS measurements of the OA formation (Supplementary Figs. 8 and 9). Gas-phase NO_3 -CIMS measurements also showed that this system generated some fast-condensing species with $\alpha > 0.1$ (Supplementary Discussion and Supplementary Fig. 10). This is much larger than the α values estimated between 0.001 and 0.002 for toluene products in previous hours-long photooxidation experiments, where α was determined by fitting SOA mass concentration profiles to the observations¹³.

Discussion

In this study, we have determined the mass accommodation coefficients for L/SVOC uptake to a variety of aerosol types in an environmental chamber by directly measuring the disappearance of oxidation products from the gas phase and their appearance in the particle phase, achieving consistent results for a wide range of compound volatilities. The accommodation coefficient, α , is generally between 0.5 and 1.0, across the large range of phases and properties of preexisting seed particles. The selected seeds span a range of viscosities and states that can be present in the real atmosphere: from low viscosity organic liquids, to semisolid or glassy α -pinene/ O_3 SOA, to solids such as AS and sucrose. The organic liquid seeds should allow compounds to very quickly diffuse throughout the particle phase after surface accommodation. For solid AS, AS/water, and sucrose, the condensed compounds likely form a layer on the surface of the seed cores⁵¹. For example, assuming a surface area per molecule of $20\text{--}40 \text{ \AA}^2$ ^{52,53} and a typical initial seed surface area of $500 \mu\text{m}^2/\text{cm}^3$, a monolayer of SOA would have a mass concentration of $\sim 0.5\text{--}1 \mu\text{g}/\text{m}^3$,

which is about 10–20% of the $\sim 5 \mu\text{g}/\text{m}^3$ of SOA formed in the AS and sucrose experiments. The formation of the first layer is expected to take up to tens of seconds, a timescale that is observed in our experiments. As illustrated by the α sensitivity test for sucrose (Supplementary Fig. 5), condensation with $\alpha = 0.1$ would be too slow to accurately simulate the measured uptake, even in the earliest stages of growth. This indicates that the α was close to 1 throughout the experiment, including during uptake onto these solid surfaces.

In addition to having different phases, the liquid and amorphous seeds used here also differ by polarity. Squalane is the least polar, AS/water and pentaethylene glycol the most polar, and the other seeds as well as the major DHN products lie in between. Despite the different seed polarities and therefore different interactions with L/SVOCs, these seeds all readily take up the L/SVOCs with similar α and timescales. We do observe differences, however, in the equilibrium gas-phase concentrations (which also appear in the model-determined c_{eff}^*), the initial amounts of SOA formed, and the evaporation rates during the 1 h measurement period (Supplementary Figs. 2a and 6).

In summary, our burst-oxidation experiments with chemically-speciated real-time molecular detection of gases and particles allow us to probe partitioning kinetics more directly than in past studies. We have found near-unity mass accommodation coefficients during G/P partitioning for representative types of aerosol that is at atmospherically relevant mass loadings (several to tens of $\mu\text{g m}^{-3}$). This potentially indicates insignificant gas-to-particle (and particle-to-gas) mass transfer limitations in the lower atmosphere at near room temperature, which supports the assumption of rapid equilibration between gases and particles currently used in atmospheric models for SOA simulation.

Methods

Chamber partitioning experiments. A series of partitioning experiments were conducted in a 20 m^3 Teflon environmental chamber. The experimental conditions were maintained at $25 \pm 0.3 \text{ }^\circ\text{C}$ and $RH < 1\%$ or $RH = 46 \pm 1\%$. We followed the experimental procedures of Krechmer et al.^{31,42}, which measured L/SVOCs partitioning to DOS particles, but with expanded seed types and new particle-phase instrumentation (Supplementary Fig. 1). First, single component seed particles were injected into a clean chamber, followed by the precursors of partitioning L/SVOCs (0.6–1.4 ppmv of 1-alkanols, and 4 ppmv each of NO and methyl nitrite). The α -pinene/ O_3 SOA as seed was formed by ozonolysis in a dark chamber 1 h before the injection of the partitioning probe compound precursors. After injection, by turning on the chamber UV black lights for precisely 10 s, the fast OH oxidation of the alkanols generated L/SVOCs at part-per-trillion by volume levels including hydroxynitrates (HNs), DHNs, CDHNS, and THNs^{31,42}. The latter three more oxidized types of L/SVOCs were monitored in the gas phase by the NO_3 -CIMS^{36,42,54}. In addition, we used EESI-MS to measure the appearance of condensed-phase DHNs and THNs. Separate analysis of the evolution of gas- and particle-phase concentrations allowed independent quantification of α for the same species. After the 10 s burst, the system was left unperturbed for 1–1.5 h, during which time the reaction products achieved equilibrium partitioning with the particles and chamber walls. Supplementary Table 1 lists the L/SVOCs that were measured by CIMS and EESI-MS and Supplementary Table 2 summarizes the experiments used for analysis.

Gas-phase measurements. The gas-phase evolution of oxidation products was monitored by a NO_3 -CIMS^{36,54}, located inside the chamber enclosure as described in Krechmer et al.³¹. A flow of 10 standard liters per minute (slpm) chamber air was delivered to the CIMS through a 0.6 m long electropolished stainless steel inlet. The concentric sample flow minimizes wall losses and does not show inlet memory effects for these semivolatile compounds^{42,54}. The total residence time in the sampling inlet and ion source was $< 4 \text{ s}$. The gaseous products were detected as NO_3^- cluster ions at a time resolution of 1 s. Background signals were checked by flowing zero air to the inlet and instrument, but were generally negligible.

Particle-phase measurements. The size distribution and number concentration of seeds and SOA were measured by a scanning mobility particle sizer (SMPS) consisting of an electrostatic classifier (TSI, 3080), differential mobility analyzer (TSI, 3081), and a condensation particle counter (TSI, 3775). The SMPS was placed inside the chamber enclosure and was operated under the same temperature and humidity as in the chamber so as not to alter partitioning states. The residence time

of air inside the SMPS at 3 lpm sheath flow rate is 7.5 s, which is short and should have a limited effect on OA evaporation, by comparison to the timescales observed in our experiments. Also the SMPS will be effectively conditioned as its surfaces are coated with SVOC during the start of an experiment, limiting evaporation on the latter part of the experiment. Each scan was performed over 120 s within the diameter range of ~16–583 nm, with 15–25 s to return to the starting voltage, resulting in a time resolution of 135–145 s. Tests of slower scan rates (up to 300 s) showed no differences in the measured distributions versus those at 120 s.

The EESI source was used with the time-of-flight mass spectrometer to monitor particle-phase semivolatile compounds^{39,55}. Air was drawn from the chamber at 3.8 lpm, of which 1 lpm passed through a gas phase denuder that removed gaseous VOCs and entered the EESI source (and 2.8 lpm were exhausted). The primary spray was generated from a solution of water–acetonitrile 1:1 mixture containing 100 ppm (by weight) sodium iodide (NaI). The collisions between particles and highly charged spray droplets dissolve particulate analytes, resulting in the formation of gas-phase ions (typically Na⁺ adducts). The measurement time resolution was also 1 s. The background of the measured compounds was determined by passing the ambient sample through a high-efficiency particle air filter, demonstrating an effective time response of ~6 s (Supplementary Fig. 11). Data analysis was conducted using DHN measurements for the five available seeded experiments (Supplementary Table 2) and THNs for the sucrose experiment. THNs were only measured at reliable S/N ratios for the sucrose-seeded EESI experiment after more extensive instrument tuning.

Kinetic modeling. A box model that includes the condensation and evaporation of oxidized products to and from particles and chamber walls was used to calculate the accommodation coefficients and effective saturation concentrations (c_{eff}^*). The model was modified from Krechmer et al.^{31,42} and was solved using the KinSim software within Igor Pro⁵⁶. As shown in Supplementary Fig. 1, the reversible vapor–wall interaction is modeled dynamically using the first-order vapor wall loss rate coefficient ($k_{G \rightarrow W}$), the vapor saturation concentration of the partitioning molecule (here c^* estimated with SIMPOL⁵⁷, referred to c_{SIMPOL}^* hereafter), and the equivalent partitioning mass of the chamber walls (C_w , $\mu\text{g m}^{-3}$). $k_{G \rightarrow W}$ and C_w were determined for our chamber by conducting the same oxidation reactions in the absence of particles⁴². The measured average $k_{G \rightarrow W}$ is $1.0 \times 10^{-3} \pm 20\% \text{ s}^{-1}$. C_w was calculated using initial and equilibrium gas-phase signals following the parameterization method in Krechmer et al.⁴² (Supplementary Fig. 3).

The rate of condensation of vapors onto particles depends on the suspended particle CS. We calculated CS using the following equation and the particle size distribution measured by an SMPS^{58,59}:

$$CS = \int_0^{\infty} r \cdot F_{\text{FS}}(r) \cdot N(r) \cdot dr, \quad (2)$$

where r is the particle radius, $N(r)$ is the particle number size distribution, and $F_{\text{FS}}(r)$ is the Fuchs–Sutugin correction for gas-phase diffusion in the transition regime⁵⁹:

$$F_{\text{FS}} = \frac{K_n + 1}{0.377K_n + 1 + \frac{4}{3}\alpha^{-1}K_n^2 + \frac{4}{3}\alpha^{-1}K_n}, \quad (3)$$

where K_n is the Knudsen number and α is the mass accommodation coefficient. In this case, α represents the accommodation of a specific gas-phase compound into a specific liquid or solid substrate, which is determined by fitting the simulated gas-phase/particle-phase concentration to the CIMS or EESI-MS measurements. Using CS, the actual rate coefficient of gases condensing on particles, $k_{G \rightarrow p}$, was calculated as^{58,59}:

$$k_{G \rightarrow p} = k_{\text{CS}} = 4\pi \cdot D \cdot CS, \quad (4)$$

where D , the molecular diffusion coefficients for studied organic nitrates, were estimated using Fuller’s semiempirical method for each species, which range from 5.9 to $7.9 \times 10^{-6} \text{ m}^2 \text{ s}^{-1}$ and average $6.8 \times 10^{-6} \text{ m}^2 \text{ s}^{-1}$ ^{60–62}. The CS was calculated for each SMPS scan (every 2 min), and then interpolated to the time base of the CIMS data (1 s).

The evaporation rate coefficient ($k_{p \rightarrow G}$) of condensed products from the aerosol was determined using partitioning theory:

$$k_{p \rightarrow G} = k_{G \rightarrow p} \frac{\overline{MW} \gamma p_{L,i}^0}{RT} \frac{1}{c_{\text{OA}}} = k_{G \rightarrow p} \frac{c_{\text{eff}}^* \overline{MW}}{C_{\text{OA}} MW_i}, \quad (5)$$

$$c_{\text{eff}}^* = \frac{MW_i \gamma p_{L,i}^0}{RT}, \quad (6)$$

where c_{OA} is the SMPS-measured aerosol organic mass concentration, a sum of organic seeds and SOA (assuming a density of 1.3 g cm^{-3} ⁶³), R is gas constant, \overline{MW} is mole-average molecular weight of the absorbing phase, MW_i is molecular weight of compound i , γ is activity coefficient, and $p_{L,i}^0$ is the saturation vapor pressure of pure compound i at temperature T . The effective saturation concentration c_{eff}^* of the compound i in the specific aerosol mixture is determined from the model fitting³¹.

The particle-wall loss rate coefficient $k_{p \rightarrow W}$ was also considered in the model. We determined this rate by fitting an exponential function to the measured decay of the seed volume concentration before photooxidation, and then assuming the seed plus condensed SOA decay at the same rate through the experiment. Care was taken to not touch or rub the Teflon bag to avoid inducing static charges during experiments, which would change the particle loss rates⁶⁴. A typical $k_{p \rightarrow W}$ value was $5 \times 10^{-5} \text{ s}^{-1}$, which corresponds to ~15% volume concentration loss in 1 h.

By fitting the simulated gas-phase/particle-phase concentration to the CIMS or EESI-MS measurements, we determined α and c_{eff}^* of each compound for each experiment. The optimization of these two parameters is a nonlinear regression problem based on minimizing the sum of the squares of the residuals (χ^2) between the logarithm of the modeled and observed species time series. This optimization was performed using the FuncFit built-in function in Igor Pro 7, which uses the Levenberg–Marquardt method. Since we conducted 2–3 CIMS experiments for a single type of seed (Supplementary Table 2), we fitted all the available experiments together (minimization of the total χ^2 of all experiments with a certain type of seed) to reduce uncertainties caused by experimental variability (Supplementary Fig. 5). Note that when simulating gas-phase measurements we fixed c_{SIMPOL}^* in the vapor–wall partitioning (as C_w was determined that way) while allowing optimization of c_{eff}^* to optimize the vapor–particle partitioning. For experiments with EESI-MS data, the particle-phase species time series alone cannot be used to constrain both α and c_{eff}^* since the total or starting concentrations of the partitioning compounds were unknown without CIMS measurements. In these cases, α was the only fitted parameter while c_{eff}^* of each species was constrained to the value determined from the CIMS experiments for the same seed. The uncertainties of the retrieved parameters were calculated by combining in quadrature those due to parametric uncertainties (2σ) with those of the statistics of nonlinear regression (2σ) (see “Methods” section).

Quantification of uncertainties for fitted α and c_{eff}^* . For the model-determined α and c_{eff}^* , we report their uncertainties by combining uncertainties that vary by partitioning species and by seed type, including the 2σ uncertainties due to the parameters used in modeling and the fitting error of the nonlinear regression (2σ). For the first type of uncertainties, we explored the effects of the following parameters: gas-phase molecular diffusion coefficient D ($\pm 30\%$), SMPS measured number size distribution $N(r)$ ($\pm 20\%$), OA mass concentration c_{OA} ($\pm 30\%$), C_w ($\pm 100\%$), the rate of particle-wall loss ($\pm 100\%$), and the vapor wall loss rate $k_{G \rightarrow W}$ ($\pm 20\%$). We confirmed that $k_{G \rightarrow W}$ and the rate of particle-wall loss have a negligible impact on α and c_{eff}^* ($< 1\%$) and thus did not include them in the uncertainty analysis. According to Eqs. (2)–(4), the values of α increase with smaller D , $N(r)$, and C_w . So we estimated upper and lower bounds of a typical range of α with D , $N(r)$, and C_w decreased and increased at the same time by their own uncertainties. Similarly, for c_{eff}^* we estimated an uncertainty of 35% by combining those of c_{OA} and $k_{G \rightarrow W}$, while other parameters have negligible impact ($< 1\%$). The overall error was then derived by combining in quadrature the uncertainties due to the above parameters and the 2σ error from nonlinear regression between the modeled and the observed time series.

Data availability

The source data in all figures are available for download at http://cires1.colorado.edu/jimenez/group_pubs.html. The modeling codes for data processing are described in the “Methods” section and are also available upon request.

Received: 16 February 2019 Accepted: 1 August 2019

Published online: 21 August 2019

References

- Jimenez, J. L. et al. Evolution of organic aerosols in the atmosphere. *Science* **326**, 1525–1529 (2009).
- Zhang, Q. et al. Ubiquity and dominance of oxygenated species in organic aerosols in anthropogenically-influenced Northern Hemisphere midlatitudes. *Geophys. Res. Lett.* **34**, L13801 (2007).
- de Gouw, J. A. Budget of organic carbon in a polluted atmosphere: results from the New England air quality study in 2002. *J. Geophys. Res.* **110**, D16305 (2005).
- Robinson, A. L. et al. Rethinking organic aerosols: semivolatile emissions and photochemical aging. *Science* **315**, 1259–1262 (2007).
- Pankow, J. F. An absorption model of the gas/aerosol partitioning involved in the formation of secondary organic aerosol. *Atmos. Environ.* **28**, 189–193 (1994).
- Donahue, N. M., Robinson, A. L., Stanier, C. O. & Pandis, S. N. Coupled partitioning, dilution, and chemical aging of semivolatile organics. *Environ. Sci. Technol.* **40**, 2635–2643 (2006).
- Kanakidou, M. et al. Organic aerosol and global climate modelling: a review. *Atmos. Chem. Phys.* **5**, 1053–1123 (2005).

8. Tsigaridis, K. et al. The AeroCom evaluation and intercomparison of organic aerosol in global models. *Atmos. Chem. Phys.* **14**, 10845–10895 (2014).
9. Patoulias, D. et al. Simulation of the size-composition distribution of atmospheric nanoparticles over Europe. *Atmos. Chem. Phys.* **18**, 13639–13654 (2018).
10. Saleh, R., Shihadeh, A. & Khlystov, A. Determination of evaporation coefficients of semi-volatile organic aerosols using an integrated volume—tandem differential mobility analysis (IV-TDMA) method. *J. Aerosol Sci.* **40**, 1019–1029 (2009).
11. Grieshop, A. P., Donahue, N. M. & Robinson, A. L. Is the gas-particle partitioning in alpha-pinene secondary organic aerosol reversible? *Geophys. Res. Lett.* **34**, L14810 (2007).
12. Grieshop, A. P., Miracolo, M. A., Donahue, N. M. & Robinson, A. L. Constraining the volatility distribution and gas-particle partitioning of combustion aerosols using isothermal dilution and thermodenuder measurements. *Environ. Sci. Technol.* **43**, 4750–4756 (2009).
13. Zhang, X. et al. Influence of vapor wall loss in laboratory chambers on yields of secondary organic aerosol. *Proc. Natl Acad. Sci. USA* **111**, 5802–5807 (2014).
14. Saleh, R., Donahue, N. M. & Robinson, A. L. Time scales for gas-particle partitioning equilibration of secondary organic aerosol formed from alpha-pinene ozonolysis. *Environ. Sci. Technol.* **47**, 5588–5594 (2013).
15. Julin, J., Winkler, P. M., Donahue, N. M., Wagner, P. E. & Riipinen, I. Near-unity mass accommodation coefficient of organic molecules of varying structure. *Environ. Sci. Technol.* **48**, 12083–12089 (2014).
16. Palm, B. B. et al. In situ secondary organic aerosol formation from ambient pine forest air using an oxidation flow reactor. *Atmos. Chem. Phys.* **16**, 2943–2970 (2016).
17. Pound, G. M. Selected values of evaporation and condensation coefficients for simple substances. *J. Phys. Chem. Ref. Data* **1**, 135–146 (1972).
18. McFeely, F. R. & Somorjai, G. A. Vaporization kinetics of hydrogen-bonded liquids. *J. Phys. Chem.* **76**, 914–918 (1972).
19. Lednovich, S. L. & Fenn, J. B. Absolute evaporation rates for some polar and nonpolar liquids. *AIChE J.* **23**, 454–459 (1977).
20. Louvaris, E. E., Karnezis, E., Kostenidou, E., Kaltsonoudis, C. & Pandis, S. N. Estimation of the volatility distribution of organic aerosol combining thermodenuder and isothermal dilution measurements. *Atmos. Meas. Tech.* **10**, 3909–3918 (2017).
21. Sinha, A. et al. Mass accommodation coefficients of fresh and aged biomass-burning emissions. *Aerosol Sci. Technol.* **52**, 300–309 (2018).
22. Shiraiwa, M., Ammann, M., Koop, T. & Pöschl, U. Gas uptake and chemical aging of semisolid organic aerosol particles. *Proc. Natl Acad. Sci. USA* **108**, 11003–11008 (2011).
23. Renbaum-Wolff, L. et al. Viscosity of alpha-pinene secondary organic material and implications for particle growth and reactivity. *Proc. Natl Acad. Sci. USA* **110**, 8014–8019 (2013).
24. Vaden, T. D., Imre, D., Beranek, J., Shrivastava, M. & Zelenyuk, A. Evaporation kinetics and phase of laboratory and ambient secondary organic aerosol. *Proc. Natl Acad. Sci. USA* **108**, 2190–2195 (2011).
25. Ye, Q. et al. Mixing of secondary organic aerosols versus relative humidity. *Proc. Natl Acad. Sci. USA* **113**, 12649–12654 (2016).
26. Maclean, A. M. et al. Mixing times of organic molecules within secondary organic aerosol particles: a global planetary boundary layer perspective. *Atmos. Chem. Phys.* **17**, 13037–13048 (2017).
27. Yatavelli, R. L. N. et al. Semicontinuous measurements of gas–particle partitioning of organic acids in a ponderosa pine forest using a MOVIE-HRToF-CIMS. *Atmos. Chem. Phys.* **14**, 1527–1546 (2014).
28. Ye, Q. et al. Following particle-particle mixing in atmospheric secondary organic aerosols by using isotopically labeled terpenes. *Chem* **4**, 318–333 (2018).
29. Gorkowski, K., Donahue, N. M. & Sullivan, R. C. Emulsified and liquid-liquid phase-separated states of alpha-pinene secondary organic aerosol determined using aerosol optical tweezers. *Environ. Sci. Technol.* **51**, 12154–12163 (2017).
30. Song, C., Zaveri, R. A., Shilling, J. E., Alexander, M. L. & Newburn, M. Effect of hydrophilic organic seed aerosols on secondary organic aerosol formation from ozonolysis of alpha-pinene. *Environ. Sci. Technol.* **45**, 7323–7329 (2011).
31. Krechmer, J. E., Day, D. A., Ziemann, P. J. & Jimenez, J. L. Direct measurements of gas/particle partitioning and mass accommodation coefficients in environmental chambers. *Environ. Sci. Technol.* **51**, 11867–11875 (2017).
32. Lopez-Hilfiker, F. D. et al. A novel method for online analysis of gas and particle composition: description and evaluation of a Filter Inlet for Gases and AEROSols (FIGAERO). *Atmos. Meas. Tech.* **7**, 983–1001 (2014).
33. Stark, H. et al. Impact of thermal decomposition on thermal desorption instruments: advantage of thermogram analysis for quantifying volatility distributions of organic species. *Environ. Sci. Technol.* **51**, 8491–8500 (2017).
34. Isaacman, G. et al. Online derivatization for hourly measurements of gas- and particle-phase semi-volatile oxygenated organic compounds by thermal desorption aerosol gas chromatography (SV-TAG). *Atmos. Meas. Tech.* **7**, 4417–4429 (2014).
35. Shrivastava, M. et al. Recent advances in understanding secondary organic aerosol: Implications for global climate forcing. *Rev. Geophys.* **55**, 509–559 (2017).
36. Jokinen, T. et al. Atmospheric sulphuric acid and neutral cluster measurements using CI-API-TOF. *Atmos. Chem. Phys.* **12**, 4117–4125 (2012).
37. Gkatzelis, G. I. et al. Gas-to-particle partitioning of major biogenic oxidation products: a study on freshly formed and aged biogenic SOA. *Atmos. Chem. Phys.* **18**, 12969–12989 (2018).
38. Lee, B. H. et al. An iodide-adduct high-resolution time-of-flight chemical-ionization mass spectrometer: application to atmospheric inorganic and organic compounds. *Environ. Sci. Technol.* **48**, 6309–6317 (2014).
39. Gallimore, P. J. & Kalberer, M. Characterizing an extractive electrospray ionization (EESI) source for the online mass spectrometry analysis of organic aerosols. *Environ. Sci. Technol.* **47**, 7324–7331 (2013).
40. Kumbhani, S. et al. New mechanism of extractive electrospray ionization mass spectrometry for heterogeneous solid particles. *Anal. Chem.* **90**, 2055–2062 (2018).
41. Lopez-Hilfiker, F. D. et al. An extractive electrospray ionization time-of-flight mass spectrometer (EESI-TOF) for online measurement of atmospheric aerosol particles. *Atmos. Meas. Tech. Discuss.* **2019**, 1–40 (2019).
42. Krechmer, J. E., Pagonis, D., Ziemann, P. J. & Jimenez, J. L. Quantification of gas-wall partitioning in teflon environmental chambers using rapid bursts of low-volatility oxidized species generated in situ. *Environ. Sci. Technol.* **50**, 5757–5765 (2016).
43. Canagaratna, M. R. et al. Chemical and microphysical characterization of ambient aerosols with the aerodyne aerosol mass spectrometer. *Mass Spectrom. Rev.* **26**, 185–222 (2007).
44. DeCarlo, P. F. et al. Field-deployable, high-resolution, time-of-flight aerosol mass spectrometer. *Anal. Chem.* **78**, 8281–8289 (2006).
45. Algrim, L. B. & Ziemann, P. J. Effect of the keto group on yields and composition of organic aerosol formed from OH radical-initiated reactions of ketones in the presence of NO_x. *J. Phys. Chem. A* **120**, 6978–6989 (2016).
46. Lim, Y. B. & Ziemann, P. J. Chemistry of secondary organic aerosol formation from OH radical-initiated reactions of linear, branched, and cyclic alkanes in the presence of NO_x. *Aerosol Sci. Technol.* **43**, 604–619 (2009).
47. Ye, J., Gordon, C. A. & Chan, A. W. H. Enhancement in secondary organic aerosol formation in the presence of preexisting organic particle. *Environ. Sci. Technol.* **50**, 3572–3579 (2016).
48. Ye, J. et al. Predicting secondary organic aerosol enhancement in the presence of atmospherically relevant organic particles. *ACS Earth Space Chem.* **2**, 1035–1046 (2018).
49. Robinson, E. S., Saleh, R. & Donahue, N. M. Probing the evaporation dynamics of mixed SOA/squalene particles using size-resolved composition and single-particle measurements. *Environ. Sci. Technol.* **49**, 9724–9732 (2015).
50. Saha, P. K. & Grieshop, A. P. Exploring divergent volatility properties from yield and thermodenuder measurements of secondary organic aerosol from alpha-pinene ozonolysis. *Environ. Sci. Technol.* **50**, 5740–5749 (2016).
51. You, Y., Smith, M. L., Song, M., Martin, S. T. & Bertram, A. K. Liquid-liquid phase separation in atmospherically relevant particles consisting of organic species and inorganic salts. *Int. Rev. Phys. Chem.* **33**, 43–77 (2014).
52. Davies, J. F., Miles, R. E., Haddrell, A. E. & Reid, J. P. Influence of organic films on the evaporation and condensation of water in aerosol. *Proc. Natl Acad. Sci. USA* **110**, 8807–8812 (2013).
53. Ruehl, C. R. & Wilson, K. R. Surface organic monolayers control the hygroscopic growth of submicrometer particles at high relative humidity. *J. Phys. Chem. A* **118**, 3952–3966 (2014).
54. Eisele, F. L. & Tanner, D. J. Measurement of the gas phase concentration of H₂SO₄ and methanesulfonic acid and estimates of H₂SO₄ production and loss in the atmosphere. *J. Geophys. Res. Atmos.* **98**, 9001–9010 (1993).
55. Chen H., Venter A. & Cooks R. G. Extractive electrospray ionization for direct analysis of undiluted urine, milk and other complex mixtures without sample preparation. *ChemComm* 2042–2044 (2006).
56. Zhe Peng, Jose L. Jimenez, (2019) KinSim: A Research-Grade, User-Friendly, Visual Kinetics Simulator for Chemical-Kinetics and Environmental-Chemistry Teaching. *Journal of Chemical Education* **96** (4):806–811
57. Pankow, J. F. & Asher, W. E. SIMPOL.1: a simple group contribution method for predicting vapor pressures and enthalpies of vaporization of multifunctional organic compounds. *Atmos. Chem. Phys.* **8**, 2773–2796 (2008).
58. Kulmala, M. & Wagner, P. E. Mass accommodation and uptake coefficients—a quantitative comparison. *J. Aerosol Sci.* **32**, 833–841 (2001).
59. Seinfeld, J. H. & Pandis, S. N. *Atmospheric Chemistry and Physics: From Air Pollution to Climate Change* 2nd edn, (John Wiley & Sons, Inc., Hoboken, New Jersey 2006).
60. Tang, M. J., Shiraiwa, M., Pöschl, U., Cox, R. A. & Kalberer, M. Compilation and evaluation of gas phase diffusion coefficients of reactive trace gases in the

- atmosphere: volume 2. Diffusivities of organic compounds, pressure-normalised mean free paths, and average Knudsen numbers for gas uptake calculations. *Atmos. Chem. Phys.* **15**, 5585–5598 (2015).
61. Fuller, E. N., Schettler, P. D. & Giddings, J. C. New method for prediction of binary gas-phase diffusion coefficients. *Ind. Eng. Chem.* **58**, 18–27 (1966).
 62. Fuller, E. N., Ensley, K. & Giddings, J. C. Diffusion of halogenated hydrocarbons in helium. The effect of structure on collision cross sections. *J. Phys. Chem.* **73**, 3679–3685 (1969).
 63. Kuwata, M., Zorn, S. R. & Martin, S. T. Using elemental ratios to predict the density of organic material composed of carbon, hydrogen, and oxygen. *Environ. Sci. Technol.* **46**, 787–794 (2012).
 64. Charan, S. M., Kong, W., Flagan, R. C. & Seinfeld, J. H. Effect of particle charge on aerosol dynamics in Teflon environmental chambers. *Aerosol Sci. Technol.* **52**, 854–871 (2018).

Acknowledgements

This work was supported by DOE (BER/ASR) grant DE-SC0016559, NSF grant AGS-1822664, and by a CIRES IRP grant. We thank Felipe Lopez-Hilfiker and Jay Slowik for useful discussions about EESI-MS operation, and Weiwei Hu, Pedro Campuzano-Jost, and Hongyu Guo for help with AMS operation.

Author contributions

X.L., J.L.J., P.J.Z., and D.A.D. designed the study. X.L. conducted experiments, led the analyses, and wrote the manuscript. J.E.K. and W.B. participated in running experiments. Z.P. participated in model development. All authors provided input in finalizing and revising the manuscript.

Additional information

Supplementary information accompanies this paper at <https://doi.org/10.1038/s42004-019-0200-x>.

Competing interests: The authors declare no competing interests.

Reprints and permission information is available online at <http://npg.nature.com/reprintsandpermissions/>

Publisher's note: Springer Nature remains neutral with regard to jurisdictional claims in published maps and institutional affiliations.



Open Access This article is licensed under a Creative Commons Attribution 4.0 International License, which permits use, sharing, adaptation, distribution and reproduction in any medium or format, as long as you give appropriate credit to the original author(s) and the source, provide a link to the Creative Commons license, and indicate if changes were made. The images or other third party material in this article are included in the article's Creative Commons license, unless indicated otherwise in a credit line to the material. If material is not included in the article's Creative Commons license and your intended use is not permitted by statutory regulation or exceeds the permitted use, you will need to obtain permission directly from the copyright holder. To view a copy of this license, visit <http://creativecommons.org/licenses/by/4.0/>.

© The Author(s) 2019